J. Fluid Mech. (2008), *vol.* 604, *pp.* 55–75.
doi:10.1017/S0022112008000979 Printed in the United Kingdom

Relaxation of a dewetting contact line. Part 2. Experiments

GILES DELON[1], MARC FERMIGIER[1], JACCO H. SNOEIJER[1,2] AND BRUNO ANDREOTTI[1]

[1]Physique et Mécanique des Milieux Hétérogènes, ESPCI, 10 rue Vauquelin, 75231 Paris Cedex 05, France

[2]School of Mathematics, University of Bristol, University Walk, Bristol BS8 1TW, UK

(Received 15 January 2007 and in revised form 8 January 2008)

The dynamics of receding contact lines is investigated experimentally through controlled perturbations of a meniscus in a dip-coating experiment. We first describe stationary menisci and their breakdown at the coating transition. Above this transition where liquid is deposited, it is found that the dynamics of the interface can be interpreted as a quasi-steady succession of stationary states. This provides the first experimental access to the entire bifurcation diagram of dynamical wetting, confirming the hydrodynamic theory developed in Part 1. In contrast to quasi-static theories based on a dynamic contact angle, we demonstrate that the transition strongly depends on the large-scale flow geometry. We then establish the dispersion relation for large wavenumbers, for which we find a decay rate σ proportional to wavenumber $|q|$. The speed dependence of σ is described well by hydrodynamic theory, in particular the absence of diverging time scales at the critical point. Finally, we highlight some open problems related to contact angle hysteresis that lead beyond the current description.

1. Introduction

Moving contact lines have been studied for more than thirty years but still constitute an open problem in fluid mechanics. The difficulty comes from the existence of six decades of length scale separating the macroscopic scale from the molecular scale that become active as soon as a contact line moves, due to viscous diffusion. This effect may be seen in the classical hydrodynamics description, where the no-slip boundary condition leads to a divergence of viscous stresses at the contact line (Huh & Scriven 1971; Dussan, V. & Davis 1974). Of course, this singularity can be avoided by considering molecular physics which goes beyond hydrodynamics, such as the description of diffuse interfaces (Pismen & Pomeau 2000), Van der Waals interactions (Teletzke, Davis & Scriven 1988), or slip at the solid substrate (Thompson & Robbins 1989; Ajdari *et al.* 1994). The latter mechanism has recently been accessed experimentally (Schmatko, Hervet & Léger 2005; Cottin-Bizonne *et al.* 2005), showing that slip really does occur and is not an ad hoc quantity to validate the hydrodynamic description. Over a large range of shear rates, the velocity v_s of the layer of liquid molecules adjacent to the wall was found to be proportional to the velocity gradient $\dot{\gamma}$,

$$v_s = \ell_s \dot{\gamma}, \tag{1.1}$$

where ℓ_s is the slip length. According to these experiments and molecular dynamics simulations (Thompson & Troian 1997; Barrat & Bocquet 1999), large slip lengths

are associated with a hydrophobic behaviour. For moderately large contact angles, the slip length is of the order of a few molecular sizes. Nevertheless, the strong viscous dissipation induces very large interface curvatures near the contact line (Voinov 1976; Cox 1986). This strongly curved region must be matched to the macroscopic flow, which is particularly challenging in the dewetting case (Eggers 2004, 2005).

On the experimental side, this problem is essentially studied by examining the macroscopic interface shape as a function of the properly rescaled contact line speed U (e.g. see Hoffman 1975; Dussan V., Rame & Garoff 1991; Le Grand, Daerr & Limat 2005), called the capillary number:

$$Ca = \frac{\eta U}{\gamma} , \tag{1.2}$$

where η and γ are viscosity and surface tension respectively. However, macroscopically observable parameters such as the dynamic contact angle are not very sensitive in distinguishing the microscopic contact line models. Golestanian & Raphael (2001*a*) proposed that by studying perturbations of contact lines, one could discriminate between different dissipation models at the contact line. Their analysis is based on the elastic-like description for static contact lines (Joanny & de Gennes 1984; de Gennes 1986*a*): a perturbation of the contact line with wavector q induces a deformation of the free surface over a distance $1/|q|$ from the contact line. This deformation results in an elastic capillary energy proportional to $|q|$. The contact line returns to its equilibrium straight configuration with a characteristic time σ^{-1}, which in the limit of small contact angles θ scales as

$$\sigma \propto \frac{\gamma}{\eta}\theta^3|q|. \tag{1.3}$$

The θ^3 dependence reflects the visco-capillary balance within the wedge of liquid bounded by the solid substrate and the free surface. Ondarçuhu & Veyssié (1991) were the first to experimentally study this dispersion relation for a static contact line and they confirmed in particular the $|q|$ dependence in the limit of large q. Marsh & Cazabat (1993) examined the relaxation of a very slowly moving contact line, distorted by an isolated chemical defect. They showed that the relaxing line profiles can be described by functions of the form $\ln(y^2 + c^2t^2)$, where y is the coordinate along the contact line and c is the characteristic speed $\propto \gamma\theta^3/\eta$. This logarithmic shape is also a direct consequence of the particular contact line elasticity (de Gennes 1986*a*).

In the case of receding contact lines, the quasi-static theory by Golestanian & Raphael (2001*a*) predicts that the relaxation time σ^{-1} increases with contact line speed. According to their theory, this relaxation time should even diverge at the dynamically forced wetting transition (or coating transition), i.e. when a steady meniscus can no longer be sustained. An intriguing consequence of this is that perturbations due to small-scale inhomogeneities of the substrate are no longer damped at the critical point, leading to a roughening of the contact line (Golestanian & Raphael 2003). This scenario contrasts with the dispersion relation obtained from the full-scale hydrodynamic calculation presented in our preceding paper (Part 1, Snoeijer *et al.* 2007), predicting a finite relaxation time for perturbations smaller than the capillary length $\ell_\gamma = \sqrt{\gamma/\rho g}$ (ρ and g denote density and acceleration due to gravity respectively). This hydrodynamic calculation explicitly accounts for viscous dissipation at all lengths and is thus expected to be more accurate than a quasi-static approach, in which dissipative effects enter through an effective boundary condition.

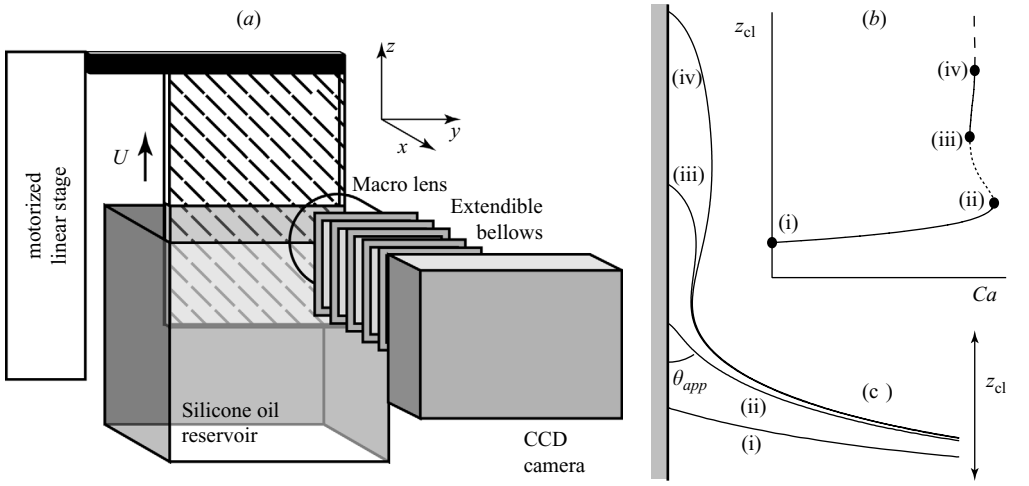

FIGURE 1. (*a*) Experimental set-up. A vertical plate is withdrawn at velocity U_p from a bath of liquid that does not spontaneously wet it. (*b*, *c*) Bifurcation scenario predicted in Part 1. By numerically solving for stationary profiles at various plate velocities, we determined the meniscus rise z_{cl} and the corresponding bifurcation diagram z_{cl} vs $Ca = \eta U_p/\gamma$. Note that the critical velocity is attained for a finite meniscus rise.

In this paper we experimentally study the global stability and relaxation times of a contact line in the context of a simple dip-coating experiment (figure 1). When a vertical plate is withdrawn from a liquid bath at velocities below the dynamical wetting transition, the contact line equilibrates at a height z_{cl} and we study the relaxation of well-controlled perturbations. We find that the relaxation times increase as the coating transition is approached. However, as we have shown previously (Snoeijer *et al.* 2006), the transition is not critical because relaxation times remain finite at threshold. The full dispersion relation is established and compared quantitatively to hydrodynamic results. Above the coating transition it is found that the upward moving contact line evolves through a succession of quasi-steady states. We can thus, for the first time, experimentally access the full bifurcation structure of the wetting transition, using these transients during liquid deposition. Our experiments confirm the non-trivial bifurcation scenario proposed in Part 1, which has been summarized in figure 1(*b*, *c*): for increasing meniscus rise z_{cl}, the corresponding velocity passes through a series of maxima and minima, denoted by (i)–(iv), each corresponding to a saddle-node bifurcation (Part 1). The maximum possible speed occurs at a well-defined value of z_{cl}.

The paper is organized as follows. In § 2 we describe briefly the experimental set-up and the physico-chemical properties of the system used. The framework of the hydrodynamic theory developed in Part 1 is briefly recalled in § 3. In § 4, we then examine the global shape of the meniscus, essentially characterized by its height above the liquid bath. We determine the critical velocity for meniscus stability, discuss the different flow structures observed experimentally, and investigate the bifurcation diagram from the transients during liquid deposition. Section 5 is devoted to the analysis of the contact line relaxation. We first examine periodic perturbations created by rows of defects moving through the contact line. These perturbations are shown to decay with a rate σ proportional to the wavenumber $|q|$, as for a static contact line. We also examine the $q = 0$ mode, i.e. the relaxation of the average meniscus height

to its stationary position. In § 6 we show that the variation of σ with respect to the capillary number and its behaviour near the coating transition are described well by the hydrodynamic theory. We complete this discussion of contact line relaxation, in § 7, by presenting experiments on localized perturbations. We conclude by addressing several open problems in contact line dynamics, in particularly the possible influence of hysteresis which has not yet been studied properly.

2. Experimental set-up

The experiment simply consists of withdrawing a partially wetting plate from a vessel filled with viscous liquid (figure 1*a*), at a constant velocity U_p. The plate is a 5 cm wide strip, cut from a silicon wafer (Siltronix). A thin layer of fluorinated material is deposited on the wafer by dip coating in a solution of FC 725 (3M) in ethyl acetate. The liquids used are polydimethylsiloxanes (PDMS, Rhodorsil 47V series) with dynamic viscosities η ranging from 1 to 5 Pa s (the corresponding average molecular weights range from 21 000 to 40 000), surface tension $\gamma = 21\,\mathrm{mN\,m^{-1}}$ and density $\rho = 980\,\mathrm{kg\,m^{-3}}$. The corresponding capillary length is $\ell_\gamma = \sqrt{\gamma/\rho g} = 1.46\,\mathrm{mm}$. This particular physico-chemical system was chosen because high-molecular-weight PDMS is non-volatile and its low surface tension inhibits rapid contamination of the free surface. In addition, this allows a direct comparison with other experiments performed with the same system in a different geometry.

PDMS is a molten polymer and it exhibits an entanglement transition at a molecular weight around 20 000 (Rahalker *et al.* 1984). The flow behaviour is Newtonian up to a critical shear rate $\dot{\gamma}_c$ which decreases with the molecular weight. For the fluids used in this study, $\dot{\gamma}_c \approx 10^4\,\mathrm{s^{-1}}$ (Lee, Polmanteer & King 1970). This critical value, above which shear thinning is observed, should be compared to the experimental shear rates at the macroscopic and microscopic scales. At the macroscopic scale $\dot{\gamma} \approx U_p/\ell_\gamma$, which never exceeds 0.1 $\mathrm{s^{-1}}$. Thus we expect a purely Newtonian behaviour of the liquid at the scale of the capillary length. At the microscopic scale $\dot{\gamma} \approx U_p/a$, where a is a molecular size of the order of 10 nm. The shear rate can thus reach $10^4\,\mathrm{s^{-1}}$ very close to the contact line and a moderate decrease of the viscosity might take place (Lee *et al.* 1970).

We were not able to measure directly the slip length of our system, but it can be estimated as follows. Starting from the length of the Si–Si binding (around 0.3 nm) and from the number of monomers (around 25^2 for the high-viscosity oil of $\eta = 4.95$ Pa s), we obtain the size of a molecule $a \simeq 7.5\,\mathrm{nm}$ (Le Grand *et al.* 2005). It is known from molecular dynamics simulations that contact angles lower than 90°, for which the interaction between the liquid and the substrate is attractive, give rise to a slip length of the order of 2 molecular lengths (Thompson & Troian 1997). Throughout the paper we therefore use the value $\ell_s \simeq 2a \simeq 15\,\mathrm{nm} \simeq 10^{-5}\ell_\gamma$ when comparing to theoretical results.

PDMS partially wets the fluorinated coating with a static contact angle that can vary from one plate to another by about 5°. The data presented here have been obtained for a receding contact angle of $\theta_r = 51.5°$ and an advancing contact angle of $\theta_a = 57.1°$. Like all the plates prepared for this study, the contact angle hysteresis is thus very low ($\theta_a - \theta_r < 7°$), as previously obtained (Rio *et al.* 2005).

To induce controlled perturbations of the contact line we create wetting defects that significantly distort the contact line as they move through the meniscus. We use two techniques:

(i) Controlled deposition of ink droplets on the fluorinated coating. When dried, ink has a much higher surface energy than the fluorinated coating, and it is completely wetted by the silicone oils.

(ii) Spin-coating a layer of photo-sensitive resin (SU-8 Microchem) on the surface of a silicon wafer. After UV exposure through a mask the resin is harderned, leaving cylindrical posts (200 μm wide, 100 μm high) on the wafer. The whole surface is then coated with FC-725, as described above. With this technique, the surface wettability is uniform and the defects are purely geometrical.

The size of the vessel containing the liquid is chosen sufficiently large ($10 \times 10\,\mathrm{cm}^2$) to avoid any capillary interaction between the meniscus on the plate and the menisci formed on the rim of the vessel. Also, the cross-section of the silicon wafer is 10^{-3} times the cross-section of the vessel, so that the liquid displacement by the wafer hardly affects the vertical position of the free surface. When the plate moves at its typical high velocity, $100\ \mu\mathrm{m\,s}^{-1}$, the reference level in the bath is displaced only at $0.1\ \mu\mathrm{m\,s}^{-1}$.

The motion of the plate is controlled within 1 μm by a motorized linear stage (Newport Corp., linear stage M-UTM50, controller ESP300). The image of the meniscus is recorded with a CCD camera (Basler A602f, 656×492 pixels, pixel size: $9.9\ \mu\mathrm{m} \times 9.9\ \mu\mathrm{m}$, $100\ \mathrm{frames\,s}^{-1}$) fitted with a macrophotography bellows and a Nikon 2.8/60 mm lens. We can thus obtain a magnification ratio of 5, in which case 1 pixel in the image corresponds to 2 μm on the object plane.

The location of the contact line is precisely determined by a cross-correlation procedure. The grey-level profile corresponding to the unperturbed contact line is recorded for each experiment. This reference profile is then correlated with each vertical line of the image. The contact line position corresponds to the location of the correlation maximum. The location of this maximum is subsequently refined with subpixel resolution by interpolation around the correlation peak. This procedure is implemented as a plugin for the ImageJ software (http://rsb.info.nih.gov/ij/).

3. Hydrodynamic framework

We now briefly describe the hydrodynamic theory to which the experimental results will be compared. We basically follow the analysis of Part 1 which is based upon the lubrication approximation for non-inertial free-surface flows (Oron, Davis & Bankoff 1997; Hocking 2001; Eggers 2004). However, to enable a quantitative comparison involving large contact angles, typically around 45°, we include corrections to the standard lubrication theory as proposed by Snoeijer (2006). The governing equations for the interface profile $h(z, y, t)$ then become

$$\partial_t h + \nabla \cdot (h\,\boldsymbol{U}) = 0, \tag{3.1}$$

$$\nabla\kappa - \boldsymbol{e}_z + \frac{3(Ca\,\boldsymbol{e}_z - \boldsymbol{U})}{h(h + 3\ell_s)} F(\theta) = \boldsymbol{0}, \tag{3.2}$$

representing mass conservation and force balance respectively. Here, $\boldsymbol{U}$ is the depth-averaged velocity, while κ is twice the mean curvature of the interface. The equations have been made dimensionless using the capillary length ℓ_γ and the capillary time $\eta\ell_\gamma/\gamma$. The equations differ from the standard lubrication approach through a correction factor

$$F(\theta) = \frac{2}{3}\frac{\tan\theta \sin^2\theta}{\theta - \cos\theta \sin\theta}, \tag{3.3}$$

where $\tan\theta$ is the local slope of the interface (Snoeijer 2006). $F(\theta) \simeq 1$ for $\theta \ll 1$. Refer to Part 1 for details of boundary conditions and the numerics of the linear stability analysis.

The theory requires two input parameters characterizing the contact line: the slip length ℓ_s, preventing a stress divergence, and a microscopic contact angle $\theta_{\rm cl}$. As argued in § 2, we can use a value $\ell_s = 10^{-5}\,\ell_\gamma$ estimated from the molecular size. Macroscopic results depend only logarithmically on the precise value of ℓ_s (Voinov 1976; Cox 1986). The microscopic contact angle is unknown *a priori*, but it is generally assumed to be equal to the equilibrium angle. For hysteretic systems, the static angle can take any value between θ_r and θ_a. Since the results are quite sensitive to this parameter, we have produced numerical curves using three different values of $\theta_{\rm cl}$: receding angle $\theta_r = 51.5^\circ$, advancing angle $\theta_a = 57.1^\circ$ and average static angle $(\theta_a + \theta_r)/2 = 54.3^\circ$.

4. Steady menisci

4.1. *Contact line position as a function of capillary number*

When the vertical plate is at rest, the liquid rises above the bath up to a height $z_{\rm cl}$, figure 1, determined by the capillary length and the contact angle according to the classical relation (Landau & Lifschitz 1959)

$$z_{\rm cl} = \ell_\gamma \sqrt{2(1-\sin\theta)}\ . \tag{4.1}$$

Here θ is the equilibrium contact angle (receding or advancing). This relation implies that a perfectly wetting liquid can achieve a maximum rise of $\sqrt{2}$ times the capillary length ℓ_γ.

When the plate is withdrawn with a velocity U_p, so that the contact line recedes with respect to the plate, the meniscus height increases to a new equilibrium value. The closed circles on figure 2(*a*) represent experimentally observed $z_{\rm cl}$ for various $Ca = \eta U_p/\gamma$, showing the increase of the meniscus rise with Ca. However, beyond a critical velocity, corresponding to a capillary number Ca^*, the meniscus no longer equilibrates but rises indefinitely. This is the signature of the dynamically forced wetting transition: in our experiments, steady menisci cannot exist beyond $Ca^* \approx 9.1 \times 10^{-3}$.

The dependence of $z_{\rm cl}$ on Ca can be compared to the predictions of hydrodynamic theory. As mentioned in § 3, the numerical curves are quite sensitive to the boundary condition of the microscopic contact angle, $\theta_{\rm cl}$. In figure 2(*a*) we therefore present numerical curves obtained using $\theta_{\rm cl} = \theta_r$, $\theta_{\rm cl} = \theta_a$ and $\theta_{\rm cl} = (\theta_a + \theta_r)/2$. The experimental points for $z_{\rm cl}(Ca)$ lie between the curves obtained with θ_r and the average static angle. It should be noted that, while we can measure the relative contact line motion with a precision of a few microns, it is much more difficult to obtain the reference level of the liquid bath, inducing uncertainty in the static angles.

There is an important discrepancy in the precise location of the transition: for all model parameters, the hydrodynamic theory predicts that the transition occurs when the meniscus reaches $z_{\rm cl} = \sqrt{2}\ell_\gamma$, the height attained by a perfectly wetting liquid (Part 1; Eggers 2004). We denote this theoretical maximum velocity as the critical point, with a critical capillary number Ca_c. In the experiments, entrainment has already occurred at $z_{\rm cl} \approx 1.1\ell_\gamma$, from which we infer that $Ca^* < Ca_c$. Below we discuss how the experimental Ca^* is related to the long time evolution of the contact line during liquid deposition.

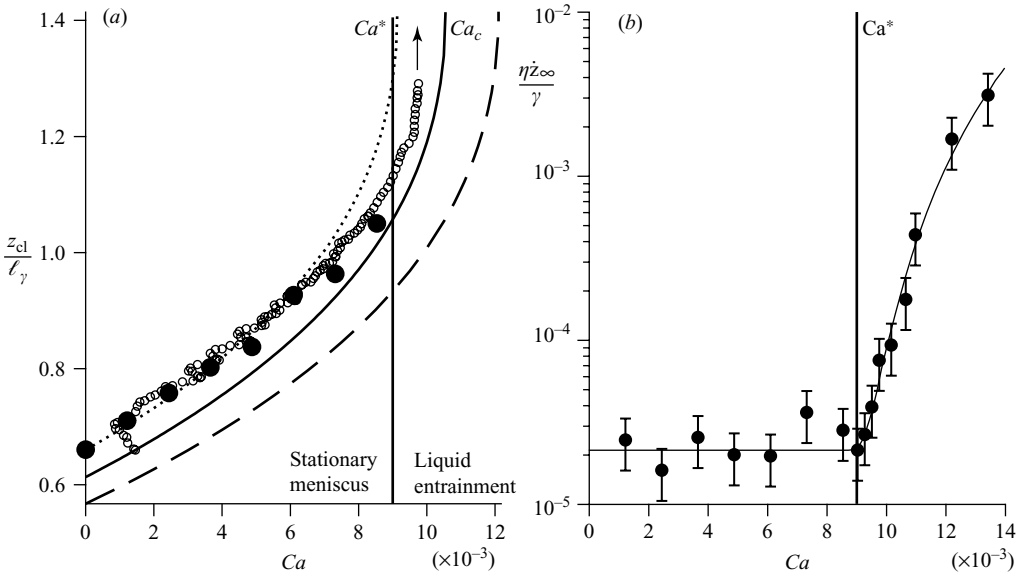

FIGURE 2. (*a*) Meniscus rise z_{cl} normalized by capillary length ℓ_γ as a function of the plate capillary number Ca. •, Steady solutions, determined experimentally as a function of Ca. ○, Rescaled meniscus rise $z_{cl}(t)$ as a function of the contact line relative capillary number $\widetilde{Ca}(t) = \eta(U_p - \dot{z}_{cl}(t))/\gamma$, for $Ca = 9.8 \times 10^{-3}$ (see text). Lines: predictions from hydrodynamic theory, with microscopic contact angle $\theta_{cl} = \theta_r$ (dotted), $\theta_{cl} = (\theta_a + \theta_r)/2$ (solid), $\theta_{cl} = \theta_a$ (dashed). (*b*) Rescaled contact line velocity at long time $\dot{z}_\infty$, as a function of the capillary number Ca. Each point corresponds to an average over several experiments. The error bars indicate the typical variation of the measured quantity from one experiment to the other. The solid line is a phenomenological fit of the form: $\eta \dot{z}_\infty/\gamma = c_1 + c_2(Ca - Ca^*)^3$. c_1 is a residual ascending velocity present even below the threshold.

These results can be represented in terms of the apparent contact angle, θ_{app}, defined from z_{cl} using (4.1),

$$\theta_{app} = \arcsin\left(1 - \frac{1}{2}\left[\frac{z_{cl}}{\ell_\gamma}\right]^2\right) . \tag{4.2}$$

As expected, this apparent contact angle decreases when the plate velocity is increased (squares, figure 3*a*). However, θ_{app} is far from zero at the coating transition, since z_{cl} remains well below the theoretical maximum of $\sqrt{2}\ell_\gamma$. Interestingly, our data for θ_{app} can be directly compared with dynamic angle measurements for the same physico-chemical system, but for a different geometry, namely droplets sliding down an inclined plane (Rio *et al.* 2005). Figure 3 shows that the two sets of data for a receding contact line are very similar, suggesting that the dynamic contact angle has some universal features. One should be careful, however, since Rio *et al.* (2005) measure the actual slope of the interface at a fixed distance from the contact line, while definition (4.2) represents an apparent slope when extrapolating static profiles.

While the behaviour of the dynamic contact angle appears to be robust with respect to the large-scale geometry, the threshold Ca for the dynamical wetting transition is far from universal. In the experiments on sliding drops performed with the same substrate and liquids, the rear of the drop assumes a conical shape such that receding contact lines move at a constant normal velocity (Podgorski, Flesselles & Limat 2001; Rio *et al.* 2005). The corresponding critical capillary number is $Ca_d = 5.7 \times 10^{-3}$, which is

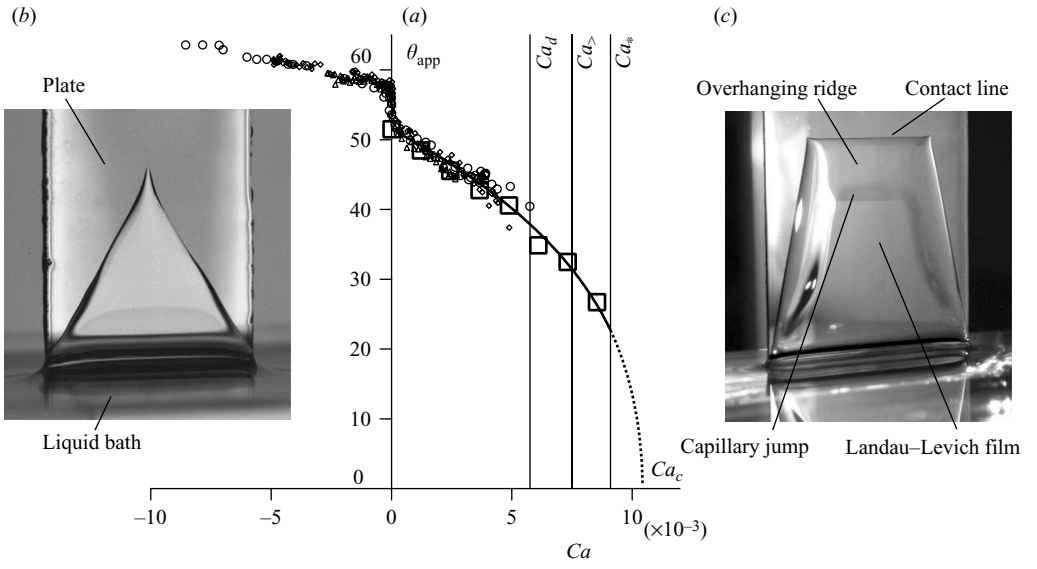

FIGURE 3. (*a*) □, Apparent contact angle θ_{app}, defined from (4.2) as a function of capillary number for PDMS on fluorinated glass or silicon. ○, ◇, △, Data from Rio *et al.* (2005) obtained for drops sliding on an inclined plane. Vertical lines indicate threshold capillary numbers Ca_d for the drop experiment, $Ca_>$ 'corner' dewetting flow on vertical plate (see text), Ca^* for the wetting transition in the plate geometry. The solid line is the result of the hydrodynamic theory for $(\theta_a + \theta_r)/2$, shifted down by 2.8°. It is mostly used as a guide for the eye but shows that the prediction is within the experimental error of the absolute position of the contact line. (*b*) Triangular liquid film observed when the dewetting lines originating at the wafer edges meet. (*c*) Overall shape of the liquid film well above the coating transition. Most of the analysis pertains to the horizontal contact line at the top of the film.

substantially lower than $Ca^* = 9.1 \times 10^{-3}$. Yet another case of inclined contact lines gives a third different value. When the plate is pulled out at $Ca > Ca^*$ the contact line becomes entrained and a film is deposited. However, while the central part of the contact line remains horizontal, no liquid entrainment occurs at the edges of the wafer. As can be seen from figure 3(*c*), this causes the contact line near the edges to incline at a well-defined angle, forming a trapezoidal shape. The sharp kinks bounding the central part move inwards during entrainment and eventually meet (figure 3*b*). The receding speed of the lateral lines was found to be $Ca_> = 7.5 \times 10^{-3}$, and thus differs from both Ca^* and Ca_d. This shows that the threshold for contact line stability is not universal but depends on the details of the large-scale geometry of the flow. We stress that apart from the reported value of $Ca_>$, all experimental results in this paper concern the central, horizontal region.

4.2. *Experimental determination of* Ca^*

The dynamical evolution from a steady meniscus towards liquid deposition provides crucial information on the wetting transition. Figure 4(*a*) shows the time evolution of the meniscus height $z_{cl}(t)$ after setting the plate velocity at a constant value at $t = 0$. When $Ca < Ca^*$, z_{cl} relaxes exponentially to a nearly flat plateau. Note that we systematically observe a very slow upwards drift at a rescaled velocity $\eta \dot{z}_\infty / \gamma \sim 2 \times \cdot 10^{-5}$, which is three orders of magnitude smaller than typical capillary numbers. Above Ca^*, the exponential relaxation is followed by a moderate rise and finally a much steeper rise corresponding to the development of the capillary ridge.

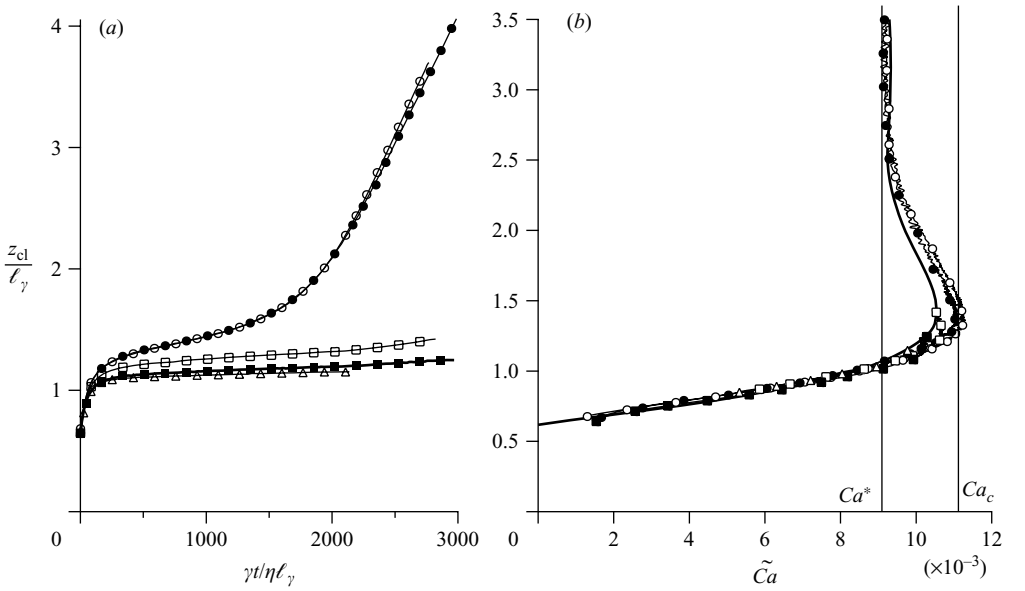

FIGURE 4. (*a*) Meniscus height z_{cl} rescaled by the capillary length as a function of time, rescaled by the capillary time for $Ca = 9.7 \times 10^{-3}$ (△), $Ca = 10.2 \times 10^{-3}$ (■), $Ca = 10.7 \times 10^{-3}$ (●), $Ca = 11.2 \times 10^{-3}$ (•) and $Ca = 11.5 \times 10^{-3}$ (○). (*b*) Same data plotted as $z_{cl}(t)$ as a function of the contact line relative capillary number $\widetilde{Ca} = \eta(U_p - \dot{z}_{cl}(t))/\gamma$. Solid line: steady solutions of the multi-scale hydrodynamic model.

Figure 2(*b*) shows that there is a well-defined point at which the contact line velocity exceeds the 'noise' level, which allows identification of the coating transition.

For $Ca > Ca^*$, liquid is entrained by the plate. As can be seen from the photograph of figure 3(*c*), the interface dynamics is not trivial: immediately behind the contact line we observe the formation of a capillary ridge. We have found experimentally that this structure travels exactly at a speed Ca^*, suggesting that the threshold of entrainment is determined by properties of the ridge (Snoeijer *et al.* (2006)). In fact, the ridge consists of two flat films that are connected through a capillary shock. The boundary conditions at the contact line select a film thickness $h \propto \ell_\gamma Ca^{*1/2}$, which is much thicker than the film connected to the bath, obeying the classical Landau–Levich scaling $h \propto \ell_\gamma Ca^{2/3}$ (Landau & Levich 1942). As explained in detail in Snoeijer *et al.* (2006), this mismatch then gives rise to the shock.

The picture that emerges is thus that, experimentally, liquid deposition occurs whenever the ridge can nucleate, even though stationary linearly stable meniscus solutions in principle exist between Ca^* and Ca_c. We believe that this avoidance of critical behaviour is due to intrinsic noise in the experiment: contact angle hysteresis is a manifestation of microscopic inhomogeneity, an effect that is not treated in the model. The observation that Ca_c is sensitive to minor changes in the microscopic θ_{cl}, and the presence of contact line drift even below the transition support this interpretation.

4.3. *Quasi-steady dynamics: bifurcation diagram*

We now argue that transient states during liquid deposition provide access to the full bifurcation structure of the wetting transition. We follow the horizontal part of the contact line, away from the edges (figure 3*c*). As can be seen from figure 4(*a*),

the contact line motion first slows down as it passes close to a steady-state solution, and subsequently accelerates towards an asymptotic speed. Similar behaviour was observed in simulations by Jacqmin (2004). The dynamical evolution towards liquid deposition can be recast in the plane ($z_{\rm cl}$, $\widetilde{Ca}$), where $\widetilde{Ca}$ is the capillary number based on the relative velocity between plate and contact line, $U_p - \dot{z}_{\rm cl}$. Figure 4(b) represents parametric plots of $z_{\rm cl}(t)$ and $\widetilde{Ca}(t)$, for different plate velocities. Surprisingly, all data points for various Ca follow a single master curve. In addition, these points accurately follow the hydrodynamic prediction for the equilibrated values of $z_{\rm cl}$ versus Ca (solid line). We stress that this correspondence is far from trivial, since the theory considers stationary rather than dynamical interface profiles. It thus seems that, experimentally, the interface evolves along these stationary solutions during liquid deposition. Roughly speaking, one can identify (i) a stable branch ($\mathrm{d}z_{\rm cl}/\mathrm{d}Ca > 0$) on which all the steady menisci are located, (ii) an unstable branch ($\mathrm{d}z_{\rm cl}/\mathrm{d}Ca < 0$) where no steady menisci can exist, but where the we observe transients, and (iii) a vertical branch at $Ca = Ca^*$ corresponding to the velocity of the capillary ridge. The hydrodynamic theory predicts a slightly more complex structure with small oscillations around the vertical asymptote, which cannot be resolved experimentally.

In addition to this correspondence, the data from the upward moving menisci can be compared to the values of $z_{\rm cl}$ for steady menisci obtained at $Ca < Ca^*$ (open circles, figure 2a). The two data sets coincide, providing further evidence that transient states are similar in nature to the steady interface profiles.

These experimental findings show that the unsteady motion of the interface during liquid deposition can be inferred quantitatively from the steady-state solutions. This strongly suggests that the dynamics proceeds through a succession of steady states, which we refer to as a *quasi-steady* behaviour. Other evidence for such quasi-steady behaviour was found for $q = 0$ perturbations (Part 1), and thus it seems to be a robust feature of the long-wavelength dynamics. Experimentally, the critical point (with a vertical tangent on the $z_{\rm cl}(Ca)$ curve) is never reached through stationary menisci. However, the transients during liquid deposition follow the complete bifurcation curve, and therefore provide an indirect measurement of Ca_c. The critical capillary number is found here to be 11.1×10^{-3}, a slightly larger value than predicted by the hydrodynamic theory.

5. Dispersion relation

Having discussed the dynamics of unperturbed menisci we can address perturbations of the contact line. As originally suggested by Golestanian & Raphael (2001a, b), these should provide a sensitive experimental probe of small-scale dynamics. In this section we consider two types of perturbations on the contact line: (i) spatially periodic perturbations with rows of equally spaced defects (finite wavenumber $|q|$), (ii) a global vertical shift of the meniscus ($q = 0$). We first describe the experimental protocols, while the experimental findings results are discussed in the following section.

5.1. *Periodic defects*

To assess the dispersion relation, σ versus q, as a function of the contact line speed, we performed systematic experiments with periodically spaced defects. A horizontal row of defects is created on the solid plate, as described in § 2. When this row of defects moves through the meniscus, it entrains drops of silicone oil out of the bath. As the defects move away from the meniscus, the threads connecting the drops to the bath pinch off leaving a few satellite droplets (figure 5a). Immediately after the release from

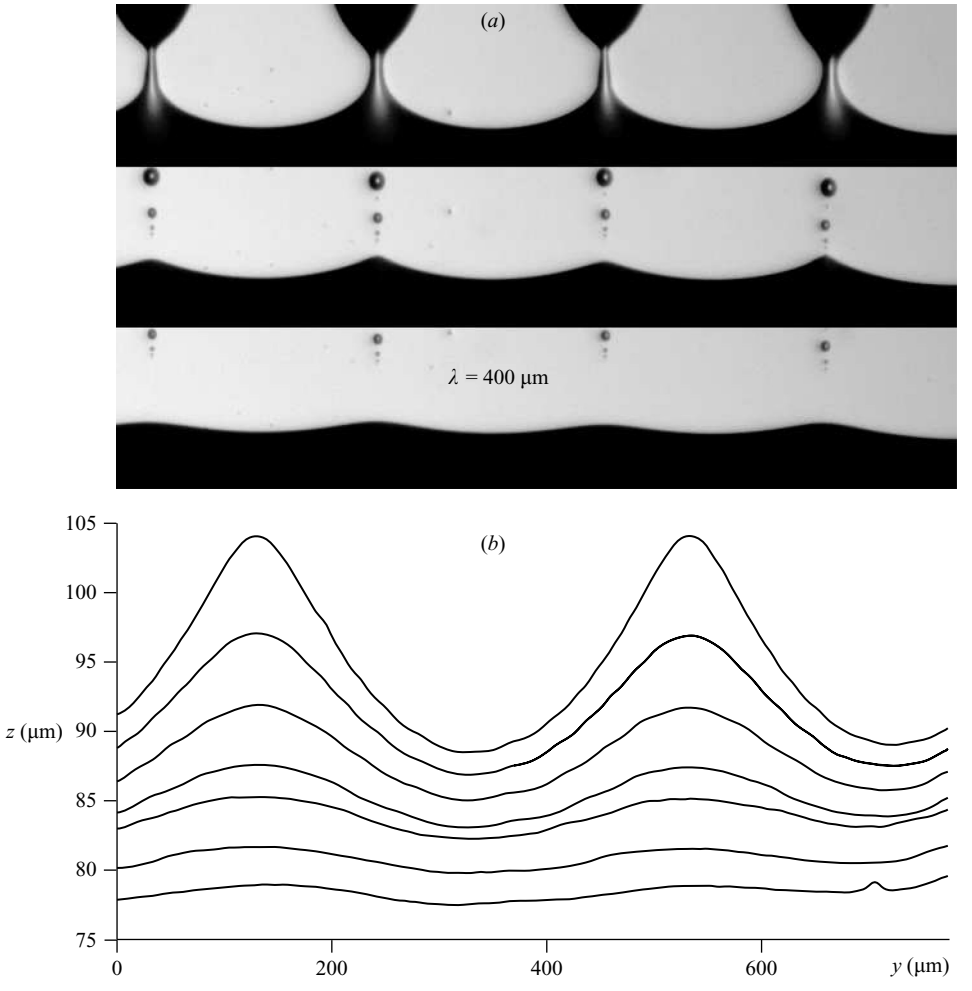

FIGURE 5. (*a*) Pictures showing the evolution of the contact line initially perturbed at wavelength $\lambda = 400\,\mu$m by chemical defects on the plate. $\Delta t = 0.4$ s. (*b*) Extracted profiles.

the defects, the contact line has a spatially periodic perturbation with sharp peaks, which decay quickly leaving a smoother almost sinusoidal perturbation. The spacing between defects is well below the capillary length, $\lambda = 400\,\mu$m or $600\,\mu$m, corresponding to $|q|\ell_\gamma \approx 23$ and 15 respectively. As a consequence, the gravitational energy involved in the meniscus deformation is much smaller than the interfacial energy.

The precise location of the contact line is determined as described in § 2 and the relaxation is analysed over a horizontal range spanning two defects (see figure 5*b*). Even though the defects are identical and evenly spaced, the liquid thread pinch-off generically does not occur simultaneously on all defects. For example, figure 5(*a*) shows the pinch-off from four defects: on the top photograph, the rightmost liquid thread is clearly wider than the middle ones. It will thus break slightly later. In the middle photograph, the corresponding peak is sharper and higher. Even after the decay of the highest spatial modes, there is still a small difference between peak amplitudes (figure 5*a*, bottom photograph). For this reason it is impossible to fit the

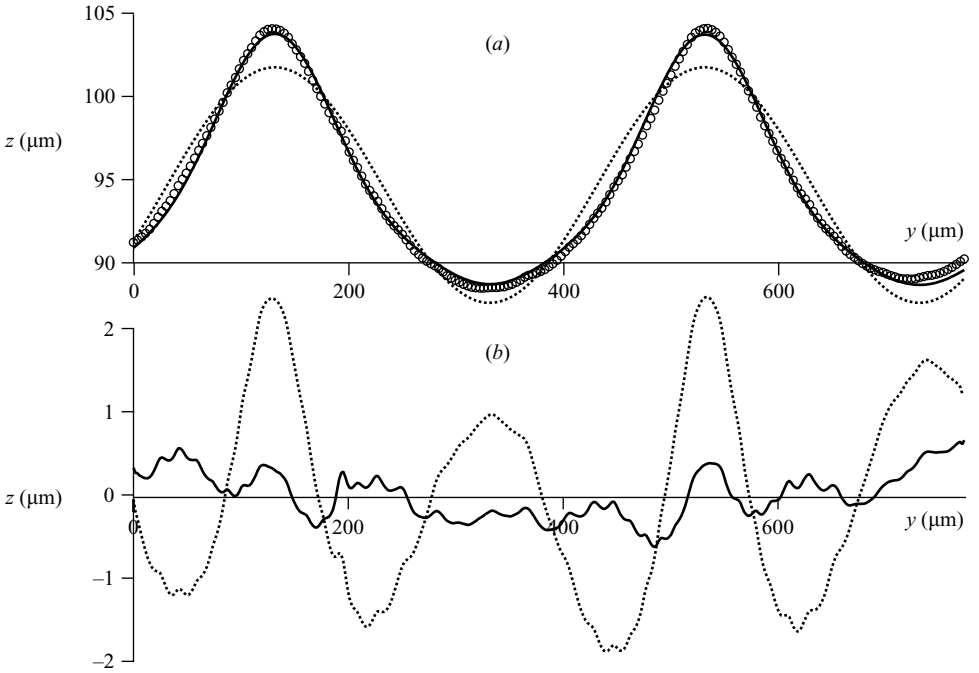

FIGURE 6. (*a*) Fit of the contact line profile (○) by a single mode of wavelength $\lambda = 400$ μm (dotted line) and by the sum of three modes, $\lambda = 400$ μm, $\lambda = 200$ μm and $\lambda = 133$ μm (solid line). (*b*) Corresponding residual ($z - z_{\mathrm{fit}}$) curves.

whole experimental curve with a single function and we choose to fit the curve in parts, considering only two defects at the same time (figure 5*b*).

To analyse the relaxation, the experimental profiles are fitted by the sum of three modes

$$z_{\mathrm{fit}} = a_0 + a_1 \cos(q_0(y-\varphi)) + a_2 \cos(2q_0(y-\varphi)) + a_3 \cos(3q_0(y-\varphi))$$

where $q_0 = 2\pi/\lambda$ is the wavenumber corresponding to the spacing λ between defects. It can be seen on figure 6 that a single cosine function does not fit the experimental curves correctly while the three-mode fit gives an accurate description: for a total amplitude of 15 μm, the difference between the experimental points and the three-mode fit is less than 0.5 μm. We thus obtain the dynamics of three different wavenumbers in a single experiment. This procedure allows a very precise determination of the amplitude (figure 7*a*), with a resolution exceeding the camera resolution. This is due to the averaging procedure which is implied by the fit over hundreds of data points.

For the three modes used in the fitting function, the amplitude decays exponentially as $e^{-\sigma t}$ (figure 7*a*), with a decay rate σ proportional to the wavenumber (mode 2 decays twice as fast as mode 1 and mode 3 three times faster than mode 1). As we will show below (figure 9*a*), the data derived from the relaxation of the perturbation from multiple defects indeed display a linear relation between the relaxation rate σ and the wavenumber $|q|$, within experimental error, as anticipated in (1.3).

5.2. *'Zero mode' relaxation*

The experiments with regularly spaced defects provide data only in the long-wavenumber limit $|q|\ell_\gamma \gg 1$. But, we can obtain information on the small-wavector

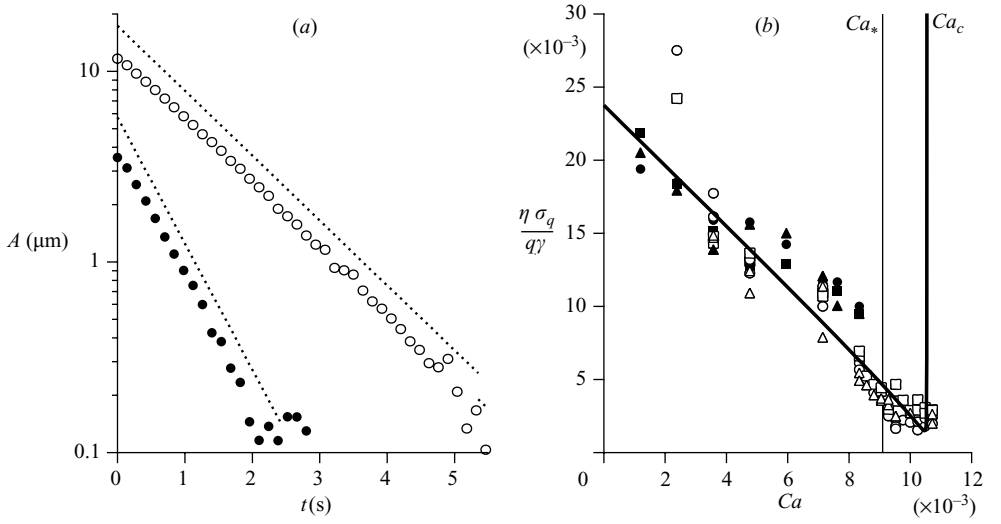

FIGURE 7. (*a*) Amplitude of contact line deformation as a function of time for periodic perturbations. Open circles $\lambda = 400\,\mu$m, filled circles $\lambda = 200\,\mu$m. The dotted lines are exponentials. (*b*) Dimensionless relaxation rate as a function of capillary number at different wavelengths (defects with 600 μm spacing: $\lambda = 600\,\mu$m (○), $\lambda = 300\,\mu$m (□), $\lambda = 200\,\mu$m (△); defects with 400 μm spacing: $\lambda = 400\,\mu$m (●); $\lambda = 200\,\mu$m (■); $\lambda = 133\,\mu$m (▲). The solid line is the prediction of the multiscale hydrodynamic model with $\theta_{cl} = (\theta_a + \theta_r)/2$.

limit $q \to 0$ simply by considering the relaxation of the meniscus height z_{cl} towards its steady value. Again, the amplitude of perturbation decays exponentially with time (figure 8*a*). We fit the curves $z_{cl}(t)$ for $Ca < Ca^*$ (as shown on figure 4*a*) by a function: $z_{fit} = (z_{cl} + \dot{z}_\infty t)[1 - e^{-\sigma t}]$, in which we account for the long-term drift of the contact line through the term $\dot{z}_\infty t$. We thus obtain the relaxation rate σ of the $q = 0$ mode as a function of the capillary number.

6. Dimensionless relaxation rates and their evolution with Ca

We now analyse the experimentally measured relaxation rate, σ, as a function of q and Ca. In order to compare this experimental dispersion relation to theoretical predictions, we define dimensionless relaxation rates with different scalings in the limits $|q|\,\ell_\gamma \gg 1$ and $|q|\ell_\gamma \ll 1$.

6.1. *Short wavelengths:* $|q|\ell_\gamma \gg 1$

Gravity plays no role in the large-wavenumber limit, so the only length scale in the problem is provided by the wavelength of the perturbation. Hence, we expect the relaxation rate to scale with the imposed deformation $|q|$ and the characteristic capillary velocity γ/η (de Gennes 1986*a*). We therefore introduce the dimensionless relaxation rate $\sigma_\infty(Ca)$:

$$\sigma = \frac{\gamma}{\eta}|q|\,\sigma_\infty(Ca), \tag{6.1}$$

where the subscript ∞ refers to the limit $q\ell_\gamma \to \infty$ (see also Part 1).

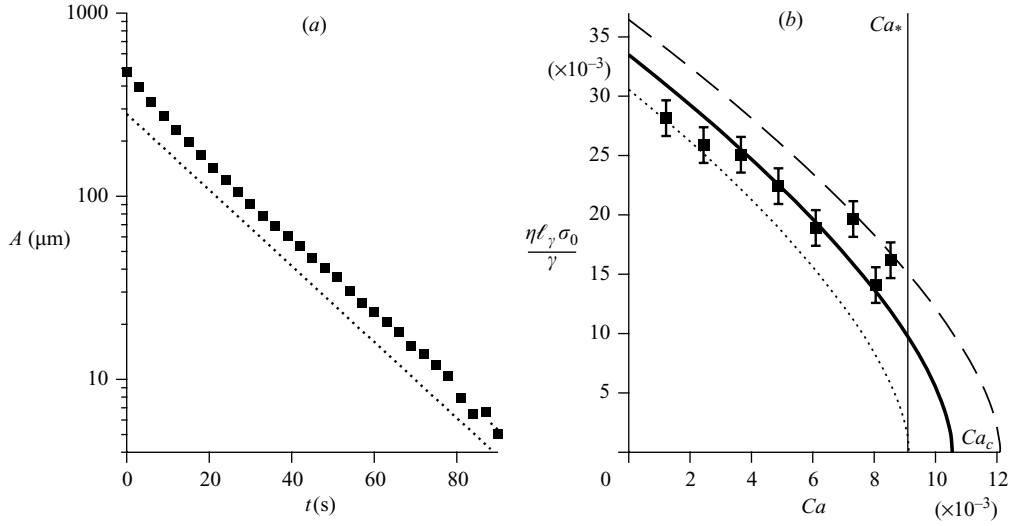

FIGURE 8. (*a*) Amplitude of contact line perturbation as a function of time for the 'zero' mode $\lambda \to \infty$. (*b*) Dimensionless relaxation rate for the zero mode as a function of capillary number. The data have been obtained with the same plate. The error bars indicate the typical variation from one experiment to the other. The lines are the prediction of the multiscale hydrodynamic model for $\theta_{\rm cl} = \theta_r$ (dotted line), $(\theta_r + \theta_a)/2$ (solid line), θ_a (dashed line).

The quasi-static theory for contact lines predicts σ_∞ in terms of the apparent contact angle $\theta_{\rm app}$ and its dependence on Ca (Golestanian & Raphael 2003)

$$\sigma_\infty = -\theta \left(\frac{{\rm d}\theta_{\rm app}}{{\rm d}Ca} \right)^{-1}, \tag{6.2}$$

which is the small-angle limit of a more general expression. For all models of $\theta_{\rm app}(Ca)$ (such as Cox 1986; Voinov 1976; de Gennes 1986*b*; Blake, Coninck & D'Ortuna 1995), σ_∞ is found to decay almost linearly with Ca, and vanishes at the critical capillary number for entrainment. This implies a diverging relaxation time σ^{-1}, a direct consequence of the diverging slope ${\rm d}\theta_{\rm app}/{\rm d}Ca$ at the critical point. The slope of the curve $\sigma_\infty(Ca)$ varies from to -2 to -4, depending on the model used (Golestanian & Raphael 2001*a*).

If we examine our experimental data (figure 7*b*), we can see that σ_∞ indeed decreases almost linearly from $Ca = 0$ to $Ca = Ca^*$, the location of the coating transition. But, this decreasing trend persists beyond Ca^* when we consider the data points obtained during the transition. As we have shown in § 4, the transients during liquid deposition quasi-steadily follow the bifurcation curve so we can effectively probe the contact line dynamics up to the critical point Ca_c. The experiments clearly show that σ_∞ does not go to zero between Ca^* and Ca_c. This experimental result is in disagreement with the quasi-static theories.

If, however, the viscous dissipation is accounted for in a hydrodynamic calculation, We recovers non-zero value of σ_∞ at the critical point (Part 1). The prediction of hydrodynamic theory is represented by the solid line in figure 7(*b*), where we took the microscopic contact angle as $\theta_{\rm cl} = (\theta_a + \theta_r)/2$. It correctly describes the variation of σ_∞ over the whole range of capillary numbers, including the non-zero value at the critical point. Note that the solid line displays a sudden divergence near Ca_c, which is due to a breakdown of the linear scaling $\sigma_q \propto |q|$ at criticality. This subtle effect is not

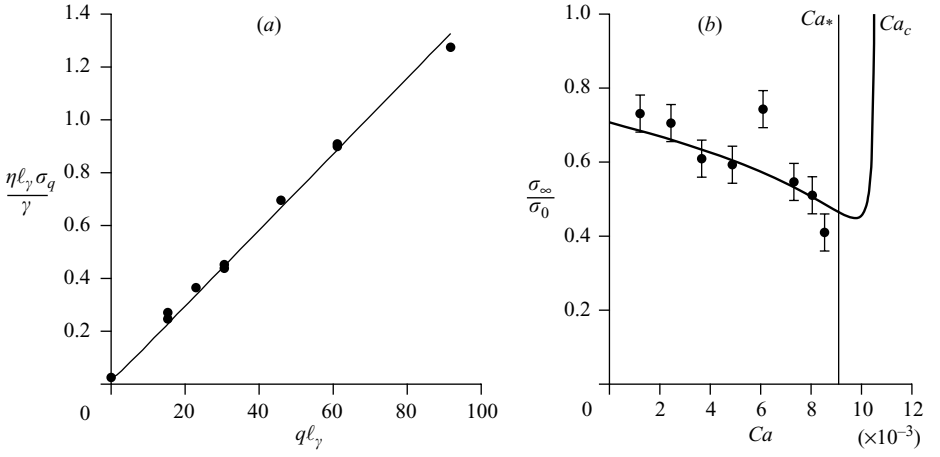

FIGURE 9. (*a*) Normalized relaxation rate as a function of the wavenumber rescaled by the capillary length. (*b*) Ratio of the relaxation rate of large-wavenumber modes to zero mode rescaled by $q\ell_\gamma$, i.e. σ_∞/σ_0. Each point corresponds to an average over several measurements. The error bars indicate the variance around the average. The hydrodynamic theory is presented by a solid line ($\theta_{cl} = (\theta_a + \theta_r)/2$).

observed in the experiments, for which the scaling with $|q|$ holds within experimental error.

6.2. *Long wavelengths:* $|q|\ell_\gamma \ll 1$

In the small-wavenumber limit, the energy of deformation is dominated by gravity and the relevant length scale is no longer provided by the wavelength, but the capillary length ℓ_γ instead (Nikolayev & Beysens 2003). We therefore define the dimensionless relaxation rate $\sigma_0(Ca)$ as

$$\sigma = \frac{\gamma}{\eta\ell_\gamma}\,\sigma_0(Ca)\ . \tag{6.3}$$

The quasi-static theory predicts a dependence with Ca of the form

$$\sigma_0 = \ell_\gamma \left(\frac{\mathrm{d}z_{cl}}{\mathrm{d}Ca}\right)^{-1}, \tag{6.4}$$

which was found in excellent agreement with the hydrodynamic calculation of Part 1. This relaxation is based on the idea that all transients with $q = 0$ effectively obey a *quasi-steady* dynamics governed by a universal curve $z_{cl}(Ca)$, a concept that we discussed already in §4. The critical point is again associated to a divergence of the slope dz_{cl}/dCa, leading to a zero value of σ_0 at Ca_c. In our experiments, we can only measure the relaxation towards a steady meniscus, i.e. when Ca remains smaller than Ca^*. Within this limit, the model accounts reasonably well for the variation of σ_0.

To close this section, let us compare the values of σ_∞ and σ_0, by plotting their ratio in figure 9*b* as a function of Ca. We find a very good agreement with hydrodynamic theory (solid line). The ratio diverges at Ca_c since $\sigma_0 \to 0$ at Ca_c, not accessible experimentally, while σ_∞ remains finite.

7. Localized perturbation and Green's function

Having confirmed the scaling $\sigma \propto |q|$ for short wavelengths, we can further investigate this "anomalous elasticity" of moving contact lines (Joanny & de Gennes 1984; de Gennes 1986*a*; Golestanian & Raphael 2001*b*). An interesting consequence of this dispersion relation is that the corresponding Green's function is a Lorentzian: a localized perturbation of the contact line, created by a single defect passing across the interface, should decay self-similarly according to a Lorentzian profile. The width (amplitude) is expected to increase (decrease) linearly in time.

Suppose that, at time 0, the contact line deformation is described by a Lorentzian of width w_0 and area A:

$$z(y,0) = \frac{A}{\pi w_0} \frac{1}{1 + y^2/w_0^2}, \tag{7.1}$$

with a peak amplitude $A/\pi w_0$. Its Fourier transform is

$$\hat{z}_q(0) = \frac{A}{\sqrt{2\pi}} \exp(-|q|w_0) \ . \tag{7.2}$$

Using (6.1), we obtain the Fourier transform after relaxation during a time t as

$$\hat{z}_q(t) = \mathrm{e}^{-\sigma t}\, \hat{z}_q(0) = \frac{A}{\sqrt{2\pi}} \exp\left(-|q| \left[w_0 + \frac{\gamma \sigma_\infty}{\eta} t\right]\right), \tag{7.3}$$

which can be inverted to

$$z(y,t) = \frac{A}{\pi w(t)} \frac{1}{1 + y^2/w(t)^2}, \tag{7.4}$$

where the width is increasing linearly in time:

$$w(t) = w_0 + \frac{\gamma \sigma_\infty}{\eta} t \ . \tag{7.5}$$

Experimentally, we thus create a very localized perturbation that should quickly evolve into a Lorentzian shape. The time evolution of the perturbation created by a single defect is shown on figure 10. In this experiment, the contact line speed is slightly below the critical speed. Immediately after depinning from the defect, the contact line is sharply peaked and cannot be fitted accurately by a Lorentzian (figure 10*b*). After a few seconds, the modes corresponding to large wavenumbers are damped and the deformation is very well approximated by a Lorentzian (for comparison we show a Gaussian fit in figure 10*c*, dotted line). It is also worth noting that a logarithmic shape resulting from a localized force applied on the contact line (de Gennes 1986*a*) cannot describe properly the experimental profiles.

The convergence to a Lorentzian shape is further shown by the rescaling of the experimental profiles $z(y,t)$, since (7.4) predicts $z(y,t)w(t)\pi/A(t) = f[y/w(t)]$. As expected, the shapes of the rescaled curves nicely collapse onto a master curve, shown on figure 11(*a*). Moreover, after the first few seconds during which the shape evolves into a Lorentzian, the computed width increases linearly with time (figure 11*b*). The spreading velocity of (7.5), $\sigma_\infty \gamma/\eta$, was found to be $17\,\mu\mathrm{m\,s^{-1}}$ in this example, corresponding to a dimensionless rate $\sigma_\infty \approx 8.4 \times 10^{-4}$. This value was obtained at $U_p = 140\,\mu\mathrm{m\,s^{-1}}$ with 1 Pa s oil, i.e. at $\mathrm{Ca} = 7 \times 10^{-3}$, very near the coating transition. The relaxation rate is indeed close to the lowest values observed with the periodic defects when Ca is between Ca^* and Ca_c. Finally, the area under the fitting curve A is found to be constant, again after the initial decay of the transient modes (figure 11*c*).

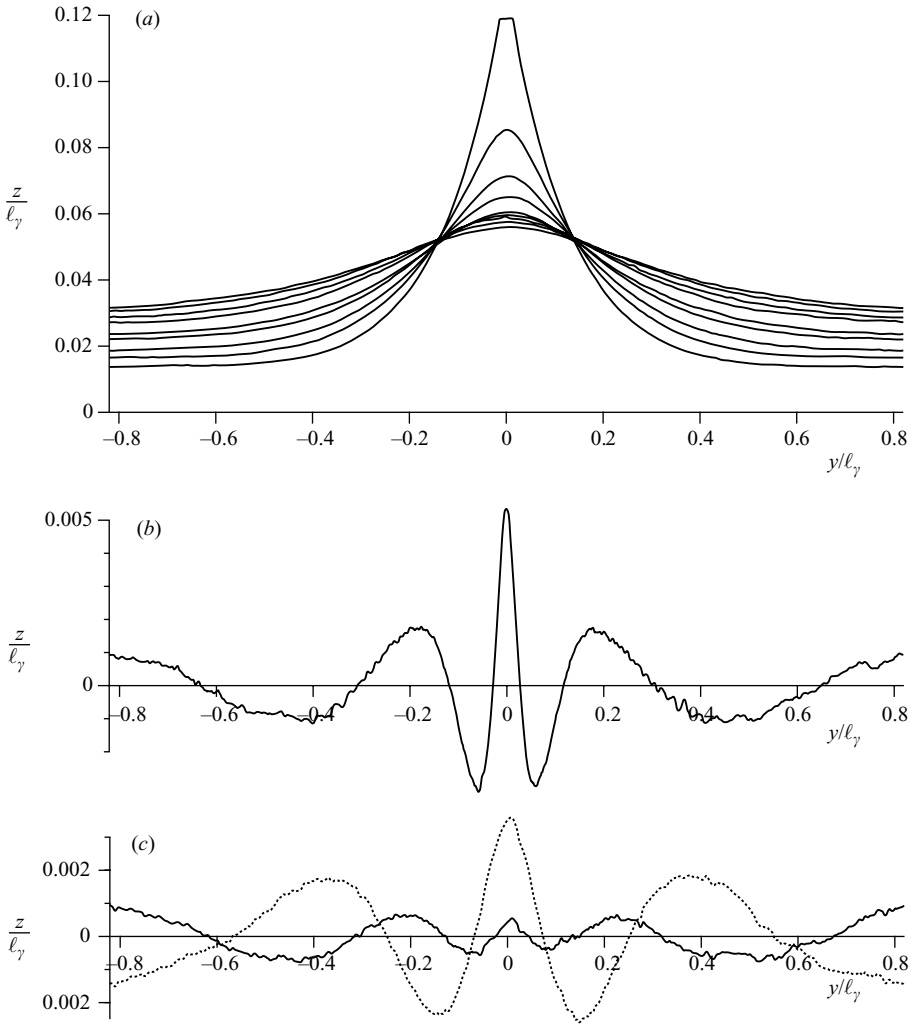

FIGURE 10. (*a*) Time evolution of the contact line initially perturbed by a single chemical defect $\Delta t = 2.5$ s, at $Ca = 7 \times 10^{-3}$. (*b*) Residual of the fit of the contact line by a Lorentzian, just after depinning ($t = 0.625$ s). (*c*) Residual of the fit of the contact line by a Lorentzian (solid line) and by a Gaussian (dotted line) at time $t = 5$ s.

8. Conclusion

We have measured the relaxation of a receding contact line, by considering perturbations in the limit of both small and large wavelengths with respect to the capillary length ℓ_γ. This provides crucial information on the dynamics of contact lines and the nature of the dynamical wetting transition. As expected from the quasi-static theory by Golestanian & Raphael (2001*a*) the moving contact line retains the particular elasticity already found for static lines, namely a relaxation rate proportional to the wavenumber $|q|$, in the limit $|q|\ell_\gamma \gg 1$. However, their crucial prediction of diverging time scales at the dynamical wetting transition is not confirmed experimentally. The initial interpretation for this was that the critical point is completely avoided through the nucleation of a capillary ridge (Snoeijer *et al.* (2006)). However, we have argued that the present experiments do explore the critical

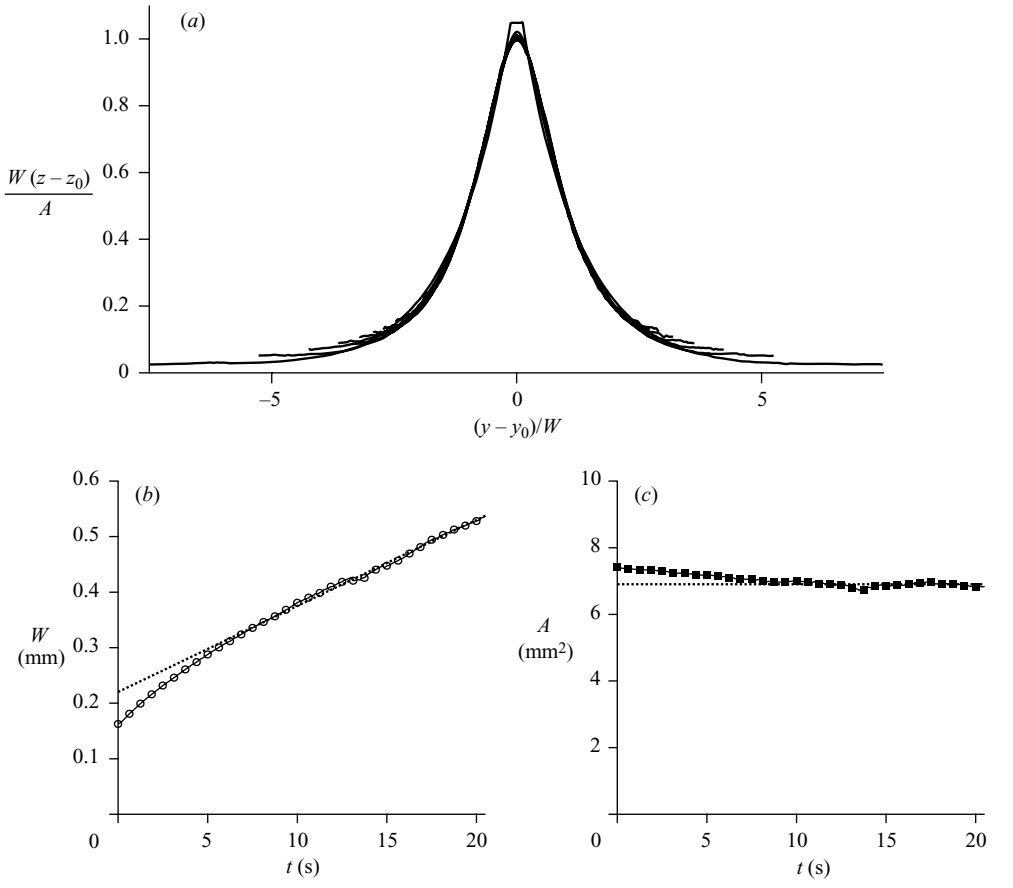

FIGURE 11. (*a*) Rescaled contact line profiles (from figure 10*a*) showing the self-similar behaviour. (*b*) Time evolution of the width derived from the fit. (*c*) Time evolution of the area A under each curve.

point through transients during liquid deposition: the interface profiles quasi-steadily proceed through stationary states, including the critical point. However there is no evidence for a diverging relaxation time for perturbations of $|q|\ell_\gamma \gg 1$, which were found to decay on a very rapid time scale even at criticality (figure 7*b*).

These findings are consistent with the hydrodynamic calculation put forward in Part 1, in which we explicitly treat viscous effects at all length scales. There we showed that the critical point is described by a standard saddle-node bifurcation, for which $\sigma = 0$ only for $q = 0$, but not for finite wave perturbations. This demonstrates that a true hydrodynamic description is crucial to unravel the dynamics of contact lines. Another conclusion of Part 1 was that stationary menisci obey a rather surprising bifurcation diagram, that is characterized by two distinct capillary numbers, Ca^* and Ca_c. The experimentally observed transient states towards liquid deposition were found to exhibit the same structure (figure 4*b*).

There is, however, an important feature missing in the hydrodynamic description. Experimentally, the coating transition occurs at Ca^*, while in theory solutions are linearly stable up to Ca_c. Sedev & Petrov (1991) studied the coating transition for small siliconized glass rods pulled out of a bath of water–glycerin mixture. Within their experimental uncertainty, they found that liquid deposition occurs when the

meniscus height is very close to its maximum value, with corresponding values of θ_{app} ranging from 2° to 13°. This is in contradiction with our results. It should be noted that their substrates exhibit a large variation of static contact angle (from 70° to 86°) and the magnitude of hysteresis is not reported. Another important difference with Sedev & Petrov (1991) is the presence of the wafer edges in our experiment. As can be seen on figure 3, oblique contact lines originate at the edges when the threshold velocity Ca^* is exceeded and we cannot exclude the possibility that this perturbation might affect the coating transition. It is thus not yet clear if the discrepancy with our results is due to the strong interface curvature in the third dimension, to hysteresis effects or to edge effects.

A crucial step would be to incorporate substrate inhomogeneities into the theory. Golestanian & Raphael (2003) discussed the influence of fluctuations of surface energy (directly correlated to hysteresis) on the stability diagram for the wetting transition. They also predict, consistent with their quasi-static theory for smooth substrates, a roughening of the contact line at the coating transition since perturbations imposed by substrate heterogeneities should no longer relax. Our experimental and theoretical findings suggest a rather different scenario at the wetting transition, and underline the need for a hydrodynamic description incorporating hysteresis.

Experimentally, it is extremely difficult to eliminate hysteresis on solid substrates. There have been attempts to use nanostructured surfaces: for example, Semal *et al.* (2000) used mixed alkanethiol monolayers to create composite surfaces with an hysteresis for alcane droplets varying from 2° to 7°. They interpreted their results of droplet spreading (measuring an apparent contact angle as a function of time) in terms of the molecular kinetic theory of Blake (Blake & Haynes (1969)). They obtained a friction coefficient for the contact line which was correlated with the average composition of the thiol monolayer. As we have shown, dynamic characteristics near transitions are much more sensitive tests than quantities like apparent contact angles which are, furthermore, ambiguously defined. It will thus be interesting to perform experiments similar to those presented here, on substrates of viscous liquids to try to eliminate the hysteresis completely, or on nano-patterned solid substrates to try to vary the hysteresis continuously.

We wish to thank Elie Raphael who initially suggested this experiment. We also thank Jose Bico, Jens Eggers and Laurent Limat for fruitful discussions and Patrice Jenffer and David Renard for technical assistance. J. H. S. acknowledges financial support from Marie Curie European Fellowships FP6 (MEIF-CT2003-502006, MEIF-CT2006-025104).

REFERENCES

Ajdari, A., Brochard-Wyart, F., De Gennes, P. G., Leibler, L., Viovy, J. L. & Rubinstein, M. 1994 Slippage of an entangled polymer melt on a grafted surface. *Physica* A **204**, 17–39.

Barrat, J.-L. & Bocquet, L. 1999 Large slip effect at a nonwetting fluid-solid interface. *Phys. Rev. Lett.* **82**, 4671–4674.

Blake, T. D. & Haynes, J. M. 1969 Kinetics of liquid/liquid displacement. *J. Colloid Interface Sci.* **30**, 421.

Blake, T. D., de Coninck, J. & D'Ortuna, U. 1995 Models of wetting: Immiscible lattice Boltzmann automata versus molecular kinetic theory. *Langmuir* **11**, 4588.

Cottin-Bizonne, C., Cross, B., Steinberger, A. & Charlaix, E. 2005 Boundary slip on smooth hydrophobic surfaces: intrinsic effects and possible artifacts. *Phys. Rev. Lett.* **94**, 056102.

Cox, R. G. 1986 The dynamics of the spreading of liquids on a solid surface. *J. Fluid Mech.* **168**, 169–194.

Dussan V., E. B. & Davis, S. H. 1974 On the motion of a fluid-fluid interface along a solid surface. *J. Fluid Mech.* **65**, 71–95.

Dussan V., E. B., Rame, E. & Garoff, S. 1991 On identifying the appropriate boundary conditions at a moving contact line: an experimental investigation *J. Fluid Mech.* **230**, 97–116.

Eggers, J. 2004 Hydrodynamic theory of forced dewetting. *Phys. Rev. Lett.* **93**, 094502.

Eggers, J. 2005 Existence of receding and advancing contact lines. *Phys. Fluids* **17**, 082106.

de Gennes, P.-G. 1986*a* Dynamique d'une ligne triple. *C. R. Acad. Sci. Paris* **302**, 731–733.

de Gennes, P.-G. 1986*b* Deposition of Langmuir-Blodget layers. *Colloid Polymer Sci.* **264**, 463–465.

Golestanian, R. & Raphael, E. 2001*a* Dissipation in dynamics of a moving contact line. *Phys. Rev.* E **64**, 031601.

Golestanian, R. & Raphael, E. 2001*b* Relaxation of a moving contact line and the Landau-Levich effect. *Europhys. Lett.* **55**, 228–234.

Golestanian, R. & Raphael, E. 2003 Roughening transition in a moving contact line. *Phys. Rev.* E **67**, 031603.

Hocking, L. M. 2001 Meniscus draw-up and draining. *Eur. J. Appl. Maths* **12**, 195–208.

Hoffman, R. L. 1975 Dynamic contact angle. *J. Colloid Interface Sci.* **50**, 228–241.

Huh, C. & Scriven, L. E. 1971 Hydrodynamic model of steady movement of a solid/liquid/fluid contact line. *J. Colloid Interface Sci.* **35**, 85–101.

Jacqmin, D. 2004 Onset of wetting failure in liquid-liquid systems. *J. Fluid. Mech.* **517**, 209–228.

Joanny, J.-F. & de Gennes, P.-G. 1984 Model for contact angle hysteresis. *J. Chem. Phys.* **11**, 552–562.

Landau, L. D. & Levich, B. V. 1942 Dragging of a liquid by a moving plate. *Acta Physicochim. URSS* **17**, 42–54.

Landau, L. D. & Lifschitz, E. M. 1959 *Fluid Mechanics*. Pergamon.

Le Grand, N., Daerr, A. & Limat, L. 2005 Shape and motion of drops sliding down an inclined plane. *J. Fluid Mech.* **541**, 293–315.

Lee, C. L., Polmanteer, K. E. & King, E. G. 1970 Flow behavior of narrow-distribution polydimethylsiloxane *J. Polymer Sci.* A2 **8**, 1909–1916.

Marsh, J. A. & Cazabat, A. M. 1993 Dynamics of contact line depinning from a single defect. *Phys. Rev. Lett.* **71**, 2433–2436.

Nikolayev, V. S. & Beysens, D. A. 2003 Equation of motion of the triple contact line along an inhomogeneous interface. *Europhys. Lett.* **64**, 763–768.

Ondarçuhu, T. & Veyssié, M. 1991 Relaxation modes of the contact line of a liquid spreading on a surface. *Nature* **352**, 418–420.

Oron, A., Davis, S. H. & Bankoff, S. G. 1997 Long-scale evolution of thin liquid films. *Rev. Mod. Phys.* **69**, 931–980.

Pismen, L. M. & Pomeau, Y. 2000 Disjoining potential and spreading of thin liquid layers in the diffuse-interface model coupled to hydrodynamics. *Phys. Rev.* E **62**, 2480–2492.

Podgorski, T., Flesselles, J. M. & Limat, L. 2001 Corners, cusps and pearls in running drops 2001. *Phys. Rev. Lett.* **87**, 036102.

Rahalker, R. R., Lamb, J., Harrison, G., Barlow, A. J., Hawthorn, W., Semlyen, J. A., North, A. M. & Pethrick, R. A. 1984 Viscoelastic studies of linear polydimethylsiloxanes *Proc. R. Soc. Lond* A **394**, 207–222.

Rio, E., Daerr, A., Andreotti, B. & Limat, L. 2005 Boundary conditions in the vicinity of a dynamic contact line: experimental investigation of viscous drops sliding down an inclined plane. *Phys. Rev. Lett.* **94**, 024503.

Schmatko, T., Hervet, H. & Léger, L. Friction and slip at simple fluid-solid interfaces: the roles of the molecular shape and the solid-liquid interaction. *Phys. Rev. Lett.* **94**, 244501.

Sedev, R. V. & Petrov, J. G. 1991 The critical condition for transition from steady wetting to film entrainment. *Colloids Surf.* **53**, 147–156.

Semal, S., Bauthier, C., Voué , M., Vanden Eynde, J. J., Gouttebaron, R. & de Coninck, J. 2000 Spontaneous spreading of liquid droplets on mixed alkanethiol monolayers: dynamics of wetting and wetting transition. *J. Phys. Chem.* B **104**, 6225

Snoeijer, J. H. 2006 Free surface flows with large slopes: beyond lubrication theory. *Phys. Fluids* **18**, 021701

Snoeijer, J. H., Andreotti, B., Delon, G. & Fermigier, M. 2007 Relaxation of a dewetting contact line. Part 1. A full-scale hydrodynamic calculation, *J. Fluid Mech.* **579**, 63–83.

Snoeijer, J. H., Delon, G., Fermigier, M. & Andreotti, B. 2006 Avoided critical behavior in dynamically forced wetting. *Phys. Rev. Lett.* **96**, 174504.

Teletzke, G. F., Davis, H. T. & Scriven, L. E. 1988 Wetting hydrodynamics. *Rev. Phys. Appl. (Paris)* **23**, 989–1007.

Thompson, P. A. & Robbins, M. O. 1989 Simulations of contact-line motion: slip and the dynamic contact angle. *Phys. Rev. Lett.* **63**, 766–769.

Thompson, P. A. & Troian S. M. 1997 A general boundary condition for liquid flow at solid surfaces *Nature* **389**, 360–362.

Voinov, O. V. 1976 Hydrodynamics of wetting. *Fluid Dyn.* **11**, 714–721.